Carbon Capture Science & Technology 2 (2022) 100028

Contents lists available at ScienceDirect

Carbon Capture Science & Technology

journal homepage: www.elsevier.com/locate/ccst

Full Length Article

Enhancement of CO_2 removal by promoted MDEA solution in a hollow fiber membrane contactor: A numerical and experimental study

Saber Kiani[a], Ahmad Taghizade[a], Rouzbeh Ramezani[b,*], Renzo Di Felice[b], Gomotsegang Fred Molelekwa[c], Saeed Mazinani[d]

[a] Arman Farayand Sanat Iranian, Jadiri Shomali Street, Tabriz, Iran
[b] Department of Civil, Chemical and Environmental Engineering, University of Genoa, Via Opera Pia, 16145 Genova, Italy
[c] Department of Environmental Health, Tshwane University of Technology, Staatsartillerie Road, Pretoria West, 0183, South Africa
[d] Department of Chemical Engineering, Centre for Advanced Separations Engineering, University of Bath, BA2 7AY Bath, U.K

ARTICLE INFO

Keywords:
MDEA
Potassium lysinate
Amino acid salt
MDEA+KLys
Nano-absorbent
ZIF-8

ABSTRACT

In this work, carbon dioxide (CO_2) loading capacity of methyldiethanolamine (MDEA) solution promoted by potassium lysinate (KLys) was experimentally measured by using a gas absorption setup at different concentrations and temperatures. The CO_2 removal efficiency of the MDEA + KLys solution was investigated for a CO_2/N_2 gas mixture by using computational fluid dynamic (CFD) simulations in a hollow fiber membrane contactor (HFMC). The effects of operating conditions including solvent concentration, solvent flow rate, gas flow rate, inlet CO_2 concentration and module length on the CO_2 removal efficiency were also studied. The experimental results revealed that CO_2 loading capacity increases with increasing KLys concentration in the solution, while decreases as temperature increases. The simulation results indicated that MDEA + KLys solution has higher CO_2 removal efficiency compared to pristine MDEA and MEA solutions. The CO_2 removal efficiency increases with increasing solvent concentration, solvent flow rate and module length, whereas decreases as gas flow rate increases. The zeolitic imidazolate framework-8 (ZIF-8), as sorbent, was then incorporated into the MDEA + KLys solution and its effect on the CO_2 removal efficiency was also examined. The MDEA + KLys + ZIF-8 nano-absorbent showed higher CO_2 removal efficiency than that of MDEA + KLys absorbent, where introducing 0.4 wt.% ZIF-8 enhanced CO_2 removal from ~96% to ~99%. The results of this work suggest that both MDEA + KLys absorbent and MDEA + KLys + ZIF-8 nano-absorbent are promising candidates for CO_2 absorption processes. However, for practical use as well as a complete investigation, their behavior should be assessed by using other parameters of solvent such as reactivity with CO_2, corrosion rate, and regeneration performance.

1. Introduction

Energy-related CO_2 emissions are expected to rise by 43% between 2008 and 2035, from 30.2 Gigatons (Gts) in 2008 to 43.2 Gts in 2035, due to high dependence on fossil fuels for economic growth (Zhang et al., 2014). With its strong relationship with climate change, and considering the effects of climate change, this phenomenon needs to be avoided or managed properly to prevent and/or minimise the environmental impacts associated with CO_2 emissions. Separation of CO_2 from large emission sources, such as flue gas from power plants, is one of the promising approaches to address the issues of CO_2 emissions and climate change. One of the predominant technologies that have been used for CO_2 capture by industry is amine-based chemical absorption (Zhang et al., 2018b), which is highly dependent on appropriate solvent to perform optimally. This factor makes the selection of an appropriate solvent important as it can have a major impact on the capital and operational cost of the process (Fang et al., 2020). Methyldiethanolamine (MDEA) is one of the attractive solvents for CO_2 absorption due to its high thermal stability, low heat of absorption and corrosion rate. However, it suffers from relatively low CO_2 absorption capacity and absorption rate (Mazinani et al., 2015).

To improve CO_2 absorption performance of amines, researchers have explored the addition of a suitable promoter, which is considered as one of the cost-effective methods. Notably, amino acid salts are promising promoters because they have high absorption capacity, high stability toward oxidative degradation and low viscosity along with high surface tension (He et al., 2017; Kumar et al., 2001; Song et al., 2012). Various amino acid salts have so far been employed as promoters in amines (Ramezani et al., 2020). For instance, potassium salts of alanine (K-Ala) and sarcosine (K-Sar) were added to piperazine (PZ) at

* Corresponding author: Dr. Rouzbeh Ramezani, University of Genoa Faculty of Engineering: Universita degli Studi di Genova Scu, Italy
E-mail address: rouzbeh.ramezani88@yahoo.com (R. Ramezani).

https://doi.org/10.1016/j.ccst.2022.100028
Received 9 October 2021; Received in revised form 3 January 2022; Accepted 4 January 2022

Nomenclature

Ni,	flux along the height of the membrane (mol $m^{-2}s^{-1}$)
Vz,	axial velocity along the length of the membrane (m s^{-1})
Ø,	volume friction of nano particles (dimensionless)
1 − α,	packing density (dimensionless)
$C_{CO2-memb}$,	concentration of CO_2 in membrane side (mol m^{-3})
$C_{CO2-tube}$,	concentration of CO_2 in tube side (mol m^{-3})
$C_{CO2-shell}$,	concentration of CO_2 in shell side (mol m^{-3})
C_i,	concentration of species i (mol m^{-3})
D_{bf},	diffusity of bulk fluid (m^2s^{-1})
D_{nf},	diffusity of nano fluid (m^2s^{-1})
d_p,	particle diameter
D_{CO2_mem},	diffusity of CO_2 in membrane (m^2s^{-1})
D_{CO2_shell},	diffusity of CO_2 in shell (m^2s^{-1})
$D_{CO2\_solvent}$,	diffusity of CO_2 in tube (m^2s^{-1})
D_{N2},	diffusity of N_2 in shell (m^2s^{-1})
Q_{in-gas},	Gas flow rate (mLmin^{-1})
T_{gas},	Gas temperature (K)
L_f,	length of HFMC (cm)
Q_{on-liq},	Liquid flow rate (mLmin^{-1})
m, CO_2	loading capacity factor (dimensionless)
n,	number of fiber (dimensionless)
P_i,	pressure of species i (Pa)
q,	langmuir isothermal adsorption model (mmol kg^{-1})
q_m,	maximum amount of adsorption by nanomaterials (mmol kg^{-1})
k_p,	langmuir constant (m s^{-1})
C_{sl},	CO_2 concentration at the solid-liquid interface (mol m^{-3})
K,	Boltzman constant (m^2 kg s^{-2} K^{-1})
Q_m,	maximum CO_2 uptake langmuir constant of ZIF-8 (mmol g^{-1})
K_d,	langmuir constant of ZIF-8 (bar^{-1})
Re,	reynolds number (dimensionless)
Sc,	schmidt number (dimensionless)
Sh,	sherwood number (dimensionless)
α_p	is the specific surface area of nanomaterials (m^2)
T_T,	temprature of gas storage tank (K)
u,	velocity variable factor (m s^{-1})
V_R	volumes of the reactor (m^3)
V_S	volumes of solution (m^3)
V_T,	volumes of gas storage tank (m^3)
z_i,	compressibility factors of CO_2 (dimensionless)
ε,	porosity of membrane (dimensionless)
μ_{nf},	dynamic voscosity of nano-absorbent (Pa s)
ρ_{nf},	density of nano-absorbent (kg m^{-3})
ρ_s,	density of solvent (kg m^{-3})
μ_s,	dynamic voscosity of solvent (Pa s)
ρ_p,	density of nanomaterials (kg m^{-3})
μ_p,	dynamic voscosity of particle (Pa s)
τ,	tortuosity of membrane (dimensionless)
$k_{CO2-mem}$,	CO_2 mass transfer caofficient (m s^{-1})
r_1,	inner radius of hallow fiber membrane contactor (mm)
r_2,	outer radius of hallow fiber membrane contactor (mm)
r_3,	outer radius of HFMC module (mm)
S,	area of vapor-liquid mass transfer interface (m^2)
U_{gas},	velocity of gas(m s^{-1})
U_{liq},	velocity of gas(m s^{-1})

different temperatures. It was found that both promoters improved CO_2 loading capacity of PZ solution (Kang et al., 2013). Sodium glycinate (SG), as the simplest amino acid salt, was added to monoethanolamine (MEA) solution. The CO_2 loading capacity of MEA + SG solution was compared with pristine MEA and the results showed that the addition of SG to MEA solution resulted in an increase in CO_2 loading capacity (Mazinani et al., 2011). CO_2 absorption performance of KLys solution in terms of absorption capacity and degradation rate was investigated. It was discovered that KLys has higher CO_2 absorption capacity, lower thermal degradation and vapor pressure, due to its ionic nature, compared to MEA (Zhao et al., 2017). In another study it was shown that KLys has a fast reactivity toward CO_2 compared to several common solvents (Shen et al., 2016). These advantages of KLys makes it an excellent candidate as an additive to amines for the enhancement of CO_2 absorption performance.

Over the recent years, many researchers have been exploring the effect of combining hollow fiber membrane contactor (HFMC) and nano-absorbents for CO_2 capture (Feron and Jansen, 2002; Peyravi et al., 2015). This technique would bring together the synergistic effect of solvents and nanomaterials into HFMCs, thus presenting the possibility of designing systems with desirable performance that cannot be achieved by conventional techniques. The nano-absorbents not only retain the benefits of the CO_2 chemisorption process, such as good CO_2 selectivity and high absorption capacity, but also show significant enhancement in mass transfer and heat transfer during CO_2 capture (Wang and Liu, 2014). Various nanomaterials, such as metal and metal oxide nanoparticles, nano-sized zeolites, covalent organic frameworks (COPs) and metal organic framework (MOFs), have been widely used in experimental and theoretical studies and showed different absorption behaviors (Yu et al., 2019; Zhang et al., 2018a). For example, iron oxide (Fe_3O_4), carbon nanotubes (CNT), silicon dioxide (SiO_2) and aluminium oxide (Al_2O_3) were incorporated into the water through a pilot-scale membrane contactor and could improve CO_2 absorption by 43%, 38%, 25% and 3%, respectively (Peyravi et al., 2015). Graphene-Oxide (GO) was added to MDEA and increased CO_2 loading capacity by approximately 9% (Irani et al., 2019).

Zeolitic imidazolate framework-8 (ZIF-8) with high-specific surface area and plenty of active surface charges has been widely used in various engineering fields such as adsorption of dyes, removal of organic chemicals and pollutants from aqueous media (Hong et al., 2016; Li et al., 2016). The favorable properties of ZIF-8 make it an interesting sorbent for integration with amines. This study presents a new approach to achieve an absorbent with high CO_2 removal efficiency by using a combination of HFMC and nanomaterials. The CO_2 loading capacity of the MDEA + KLys solution was measured using a gas absorption rig at different concentrations and temperatures. ZIF-8, was then added to the MDEA + KLys solution and performance of MDEA + KLys absorbent and MDEA + KLys + ZIF-8 nano-absorbent in terms of CO_2 removal efficiency was investigated for a CO_2/N_2 gas mixture by using CFD simulations in a HFMC. The effects of operating conditions including solvent concentration, solvent flow rate, gas flow rate, inlet CO_2 concentration and module length on the CO_2 removal efficiency were also studied. To the best of our knowledge, no study has been conducted on CO_2 absorption using MDEA promoted by KLys and ZIF-8 in a HFMC.

2. Experimental method

2.1. Materials

The detailed information of all the chemicals and gases used in this work are listed in **Table 1**.

The molecular structures of lysine, MDEA and ZIF-8 are shown in **Fig. 1**. The potassium lysinate was prepared by neutralizing the lysine with an equimolar amount of potassium hydroxide (KOH) in a volumetric flask.

Table 1
Specification of chemicals and gases used in this work.

Chemical name	Abbreviation	Source	CAS Num.	MW (g mol^{-1})	Purity[a] (%)
N-methyl-diethanolamine	MDEA	Alfa Aesar	105-59-9	119.17	> 98.0
L-Lysine	Lys	Acros	56-87-1	146.19	98.0
Potassium hydroxide	KOH	Alfa Aesar	1310-58-3	56.11	85.0
Carbon dioxide	CO_2	Air Liquide	124-38-9	44.01	99.0
Nitrogen	N_2	Air Liquide	7727-37-9	28.01	99.0

[a] The purity in mass fraction was provided by the supplier. All chemicals were used without further purification.

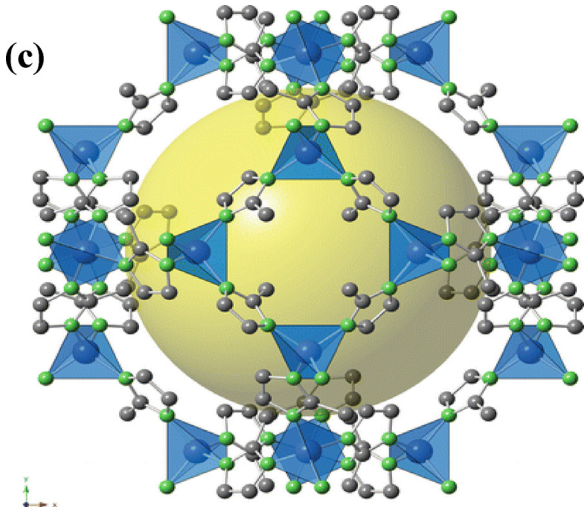

Fig. 1. Molecular structure of the (a) KLys; (b) MDEA; and (c) ZIF-8 adopted from (Hara, 2016), Black and green dots represent the carbon and nitrogen atoms, respectively. Blue polyhedrons stand for the Zn ions. All hydrogen atoms are excluded here. The yellow sphere stands for the largest van der Waals sphere enclosed in the central pore of ZIF-8.

2.2. CO2 loading capacity

The CO_2 loading capacity measurements were carried out by using a gas absorption setup that is shown in **Fig. 2**. The equipment description and calculation of CO_2 loading capacity are explained elsewhere (Ramezani and Di Felice, 2019; Ramezani et al., 2018). The rig consists of a 1 L reactor, pressure transmitter (accuracy, ± 0.15% FS), temperature sensor (uncertainty of ± 0.1 K), two impellers, vacuum pump, gas storage tank, gas cylinders and water bath (uncertainty of ± 0.1 K).

Before starting the experiment, N_2 is supplied to the reactor to remove any trace gases. The fresh solvent is fed into the reactor and then a vacuum pump is used to remove N_2. The fresh solvent was allowed to reach the desire temperature and the pressure and temperature measurements are recorded using sensors. The system is left to reach equilibrium and vapor pressure of solvent (P_V) is recorded. At stable pressure and temperature, CO_2 is introduced from the gas storage tank to the reactor. The total moles of CO_2 injected into the reactor from gas storage tank is calculated using equation (1).

$$\left(n_{CO_2}\right)_i = \frac{V_T}{R\,T_T}\left(\frac{P_1}{z_1} - \frac{P_2}{z_2}\right) \tag{1}$$

where T_T is temperature (K) and V_T is volume of gas storage tank (L). P_1 and P_2 are initial and final pressure of CO_2 in the gas storage tank before and after injection of CO_2 to the reactor, respectively. Z_1 and Z_2 refer to the CO_2 compressibility factors at pressures P_1 and P_2, respectively. The compressibility factors of CO_2 were calculated using the Peng-Robinson equation of state (Peng and Robinson, 1976). The reactor is then allowed to reach the vapor-liquid equilibrium. Thereafter the total pressure in the reactor is recorded (P_{tot}). The total moles of CO_2 that remains in the reactor $(n_{CO_2})_f$ is calculated by equation (2).

$$\left(n_{CO_2}\right)_f = \frac{(P_{tot} - P_V)\,(V_R - V_S)}{R\,T_R\,Z_3} \tag{2}$$

where V_R and V_S are the volumes of the reactor (L) and solvent (L), respectively. Z_3 is the CO_2 compressibility factors at final pressure. The CO_2 loading capacity (α) of MDEA + KLys solutions at different temperatures and different KLys concentrations was obtained using equation (3).

$$\alpha = \frac{\left(n_{CO_2}\right)_i - \left(n_{CO_2}\right)_f}{n_{MDEA+KLys}} \tag{3}$$

3. Model development

A two-dimensional (2D) axisymmetric model was developed in a cylindrical coordinate system. **Fig. 3** shows a schematic diagram of the HFMC that was used in this work for numerical modeling. The HFMC comprised of three different domains: shell and tube as well as membrane sides (Rezakazemi et al., 2012; Shirazian et al., 2012a). The governing momentum and mass transfer equations for each section of the model are expressed in section 3.1 and 3.2, respectively. In this model, the solvent flows into the tube side at $z = 0$, whereas the gas mixture flows counter-currently through the shell side of the HFMC at $z = L_f$. The model considers the non-wetting condition where the pores are not wetted by solvent.

The chemical and physical properties along with the working conditions of the HFMC are presented in **Table 2**.

The particle-particle and particle-liquid interactions can be neglected, due to low amount of nanomaterials. The laminar parabolic velocity distribution was employed for the solvent flow in the tube side while the gas flow in the shell side was defined by means of Happel's free surface model (Huang and Zhang, 2013). The following assumptions were made in this work:

- Steady-state and isothermal conditions.
- Incompressible and Newtonian fluid flow for the liquid phase.
- Radial convection is negligible.
- The gas phase is an ideal gas.
- The application of Fick's diffusion to represent the membrane mass transfer.
- Membrane pore distribution is assumed to be uniform.

3.1. Momentum equation

3.1.1. Shell side

Assuming Happle's free surface model, the velocity profile in the shell was determined using equation (4) (Happel, 1959):

$$V_{z-shell} = 2u\left[1 - \left(r_2/r_3\right)^2\right] \times \frac{\left(r/r_3\right)^2 - \left(r_2/r_3\right)^2 + 2\ln\left(r_3/r\right)}{3 + \left(r_2/r_3\right)^4 - 4\left(r_2/r_3\right)^2 + 4\ln\left(r_2/r_3\right)} \tag{4}$$

where u and r_2 are velocity ($m\ s^{-1}$) and outer hollow fiber radius (mm), respectively. Happle's free surface radius, r_3, is defined using

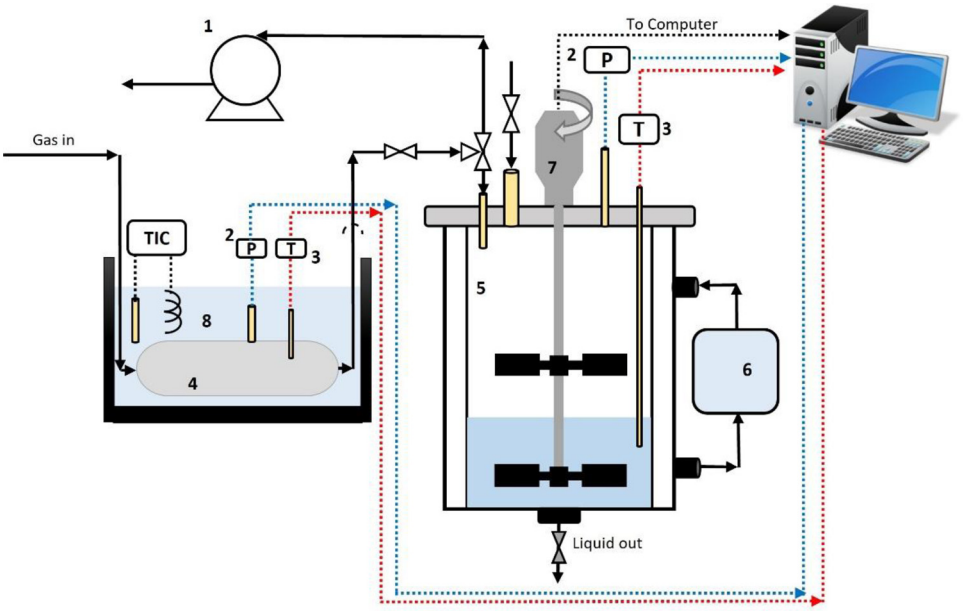

Fig. 2. Schematic diagram of the gas absorption setup: 1) vacuum pump; 2) pressure transmitter; 3) temperature indicator; 4) gas storage tank; 5) equilibrium cell; 6) heat jacket connected to water bath; 7) external magnetic stirrer; 8) water bath.

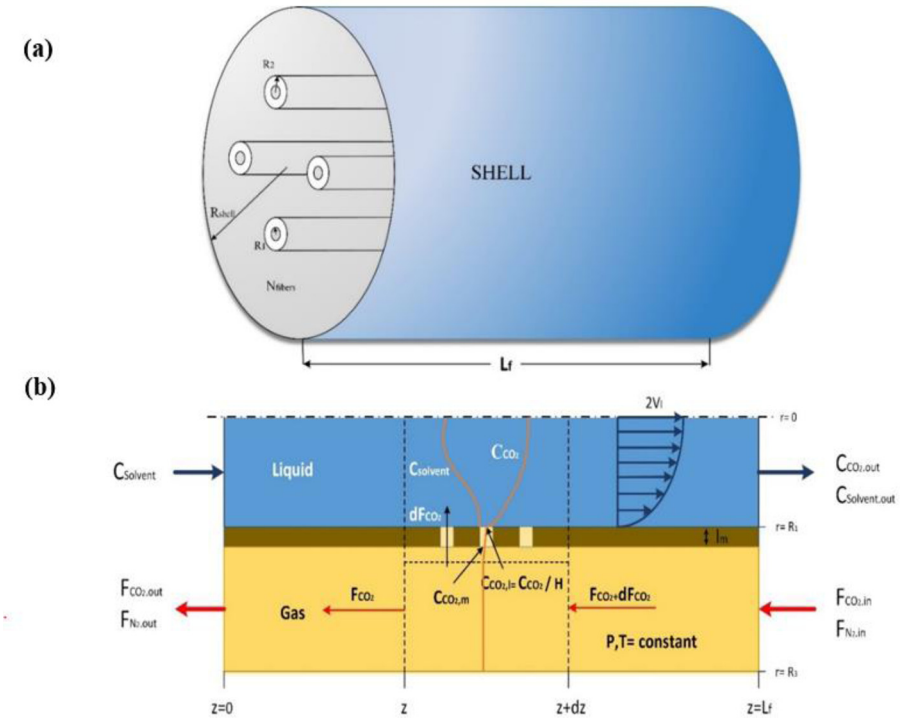

Fig. 3. The schematic of the HFMC used in the model (a) geometry; (b) gas and liquid behavior

equation (5) (Happel, 1959):

$$r_3 = r_2 \times \left(\frac{1}{1-\alpha}\right)^{0.5} \tag{5}$$

where α and 1 – α are the volume fraction of the void and packing density of HFMC respectively.

3.1.2. Tube side

The CO_2 continuity equation for the liquid phase in the tube side can be expressed using equation (6) [31]:

$$V_{z-tube} = \frac{2Q_{in\_liq}}{n\pi r1^2}\left[1-\left(\frac{r}{r_1}\right)^2\right] \tag{6}$$

where Q_{in_liq} is the volumetric liquid flow rate in the tube side ($mL\ min^{-1}$), n is the number of hollow fibers and r is the inner radius of the hollow fiber (mm).

The density of the nano-absorbent was determined using equation (7) (Yu et al., 2019):

$$\rho_{nf} = \rho_s\left(1-\varphi_p\right) + \rho_p\varphi_p \tag{7}$$

where ρ_s is the density of solvent ($kg\ m^{-3}$), ρ_p is the density of particle ($kg\ m^{(-3)}$), and φ_p is the volume fraction of nanomaterials.

Table 2
The chemical and physical properties along with the working conditions of the HFMC

Parameter	Unit	Value	Ref.
Inner hollow fiber radius, ($r1$)	mm	0.32	(Rezakazemi et al., 2019)
Outer hollow fiber radius, ($r2$)	mm	0.45	(Rezakazemi et al., 2019)
Length of fiber, (L_f)	cm	40	(Rezakazemi et al., 2019)
Number of fiber (n)	-	590	(Nakhjiri and Heydarinasab, 2020)
Porosity (ε)	-	0.52	(Nakhjiri and Heydarinasab, 2020)
Mass transfer coefficient (k_m)	$m\ s^{-1}$	$D_{co2\_shell}.\varepsilon\ (\tau.\delta)^{-1}$	(Rezakazemi et al., 2019)
Gas flow rate (Q_{in_gas})	$mL\ min^{-1}$	100	(Nakhjiri and Heydarinasab, 2020)
Inlet CO_2 concentration (C_0)	ppm	1400	(Rezakazemi et al., 2019)
Gas temperature (T_{gas})	K	298	This study
D_{CO2_shell}	$m^2\ s^{-1}$	1.33e-5	(Rezakazemi et al., 2019)
D_{CO2_mem}	$m^2\ s^{-1}$	$D_{co2\_shell}\ \varepsilon\ \tau^{-1}$	(Ghasem, 2019b)
D_{N2}	$m^2\ s^{-1}$	4e-5	(Ghasem, 2019b)
$D_{CO2\_solvent}$	$m^2\ s^{-1}$	9e-10	(Nakhjiri and Heydarinasab, 2020)
CO_2 loading factor (m)	$mol\ CO_2\ mol\ solvent^{-1}$	0.788	This study
Liquid flow rate (Q_{in_liq})	$mL\ min^{-1}$	25	(Nakhjiri and Heydarinasab, 2020)
Pressure (P_t)	bar	1	(Ghasem, 2019b)
Physical properties of solvent(20 wt% MDEA + 10 wt% KLys)			
Density of solvent	$g\ cm^{-3}$	1.0291	This study
Viscosity of solvent	$mPa.s$	1.9417	This study
Adsorption properties of ZIF-8	-		
Q_m	$mmol\ g^{-1}$	11.77	(Yang et al., 2014)
K_d	bar^{-1}	0.071	(Yang et al., 2014)
Density of particle	$gr\ cm^{-3}$	0.96	(Hunter-Sellars et al., 2021)

3.2. Mass transfer equation

3.2.1. Shell side

The continuity equation for each species without chemical reaction can be expressed using equation (8) (Hashemi et al., 2012):

$$-\nabla N_i = V_z \frac{\partial C_i}{\partial z} \tag{8}$$

where N_i, V_z, C_i and z are the flux ($mol\ m^{-2}s^{-1}$), axial velocity ($ms^{(-1)}$), concentration ($molm^{(-3)}$), and axial coordinate in the length of the membrane (m), respectively. Either Fick's law of diffusion or Maxwell-Stefan theory can be used for the calculation of flux of species i; therefore, continuity equation for CO_2 inside the shell can be expressed using equation (9) (Rezakazemi, 2018):

$$D_{CO2-shell}\left(\frac{1}{r}\frac{\partial}{\partial r}\left(\frac{r\,\partial C_{CO2-shell}}{\partial r}\right)+\frac{\partial^2 C_{CO2-shell}}{\partial z^2}\right)=V_{z-shell}\frac{\partial C_{CO2-shell}}{\partial z} \tag{9}$$

where $D_{CO2-shell}$, $C_{CO2-shell}$, $V_{z-shell}$ are diffusion coefficient of CO_2 in shell side ($m^2s^{(-1)}$), concentration ($molm^{(-3)}$) and axial velocity ($ms^{(-1)}$) respectively.

The corresponding boundary conditions are as follows:

at $z = 0$ $\frac{0(\partial^2 C_{(CO2-shell)})}{(\partial z^2)} = 0$ (a)

at z = H $C_{CO2-shell} = C_0$ (b)

at $r = r_2$ $D_{CO2-shell}\left(\frac{\partial C_{CO2-shell}}{\partial r}\right) = D_{CO2-memb}\left(\frac{\partial C_{CO2-membrane}}{\partial r}\right)$ (c)

at $r = r_3$ $\left(\frac{\partial C_{CO2-shell}}{\partial r}\right) = 0$ (d)

3.2.2. Membrane side

The steady-state balance for CO_2 transport inside the membrane, due to diffusion in the gas phase, could be represented using equation (10) (Shirazian et al., 2012b):

$$D_{CO2-membrane}\left(\frac{1}{r}\frac{\partial}{\partial r}\left(\frac{r\,\partial C_{CO2-membrane}}{\partial r}\right)+\frac{\partial^2 C_{CO2-membrane}}{\partial z^2}\right)=0 \tag{10}$$

where the concentration and diffusion coefficient of CO2 across the HFMC are respectively defined as C_{CO_2-mm} and D_{CO_2-mem}. The corresponding boundary conditions are as follows:

at $z = 0$ Insulated (a)

at $z = H$ Insulated (b)

at $r = r_1$ $C_{CO2-memb} = C_{CO2-tube}/m_{CO2}$ (c)

at $r = r_2$ $C_{CO2-memb} = C_{CO2-shell}$ (d)

The mass transfer coefficient of CO_2 in the membrane compartment of microporous membrane contactor ($k_{CO2-mem}$) is derived from equation (11) (Nakhjiri and Heydarinasab, 2020):

$$k_{CO2-mem} = \frac{D_{CO2-shell}\cdot}{\tau\sigma} \tag{11}$$

m is defined as dimensionless CO_2 loading capacity of solvent which is a function of Henry constant. In this work, m was determined experimentally through vapor-liquid equilibrium data (section 4.1). When no experimental data are available, m could be determined theoretically using equation (12) (Portugal et al., 2009):

$$m = 8.314\ \frac{T_{gas}}{H_{CO_2\_solvent}} \tag{12}$$

where T_{gas} (K) is the gas temperature.

3.2.3. Tube side

The addition of nanomaterials will result in an increase in solute mass transfer across the gas-liquid interface (Mohebbi-Kalhori et al., 2020). In this regard, some possible mechanisms have been reported. The first mechanism could be explained by Brownian motion (Bahmanyar et al., 2014; Nagy et al., 2007), where velocity disturbance field created by the micro-convection of nanomaterials increases the diffusion coefficient. An empirical equation has been recently reported, where the diffusion coefficient is defined using equation (13):

$$D_{nf} = D_{bf}\left(1 + m_1 Re^{m2} Sc^{m3} \emptyset^{m4}\right) \tag{13}$$

where $m_1 = 1650$, $m_2 = 0.039$, $m_3 = -1.064$, $m_4 = 0.203$ [34, 35], $\emptyset$ is the volume fraction of the nanomaterials, Re and Sc are the Reynolds

and Schmidt numbers respectively, for the nanomaterials Brownian motion (Prasher et al., 2005). Re value can be determined using equation (14):

$$Re = \sqrt{\frac{18KT\rho^2}{\pi d_p \rho_p \mu^2}} \tag{14}$$

where K, T, ρ, ρ_p, d_p and μ are Boltzman constant ($m^2\ kg\ s^{-2}\ K^{-1}$), temperature (K), fluid density (kg/m^3), nanomaterials density (kg/m^3), nanomaterials diameter (nm), and dynamic viscosity (($Pa\ s$)) of the fluid, respectively. The second proposed mechanism that can influence mass transfer enhancement is Grazing effect or shuttle effect mechanism (Alper et al., 1980; Golkhar et al., 2013). Grazing is a phenomenon whereby gas is being transported from the liquid-gas interface to the liquid bulk. To study this effect, the liquid phase was considered as distinct liquid and solid phases, therefore the continuity governed each phase (i.e., the absorbent and the nanomaterials), separately. The continuity equation for CO_2 in the solid phase can be described using equation (15) (Rezakazemi et al., 2019; Sumin et al., 2013):

$$\emptyset \rho_p V_z \frac{\partial q}{\partial z} = k_p \alpha_p \left(C_{CO2-tube} - C_{Sl}\right) \tag{15}$$

where $\alpha_p$is the specific surface area of nanomaterials (m^2) and $k_p$is the mass-transfer coefficient between solid particles and the liquid phase ($m\ s^{-1}$) given by equation (16) (Ghasem, 2019a; Rezakazemi et al., 2019):

$$Sh = \frac{k_p d_p}{D_{CO2}} = 2 + 0.552 Re^{0.5} Sc^{0.33} \tag{16}$$

where Sh, Re and Sc are the Sherwood number, the Reynolds number, and the Schmidt number, respectively. The value of Sherwood was found to be 2.04.

q is the amount of CO_2 adsorbed by the nanomaterials ($mmol\ kg^{-1}$) which could be obtained using Langmuir isothermal adsorption model as given in equatin (17) (Rezakazemi et al., 2019):

$$q = q_m \frac{k_d C_{Sl}}{1 + k_d C_{Sl}} \tag{17}$$

where $q_m$is the maximum amount of adsorption by nanomaterials ($mmol\ kg^{-1}$), k_d is Langmuir constant (bar^{-1}), and C_{sl} is the CO_2 concentration at the solid-liquid interface ($mol\ m^{-3}$). The CO_2 continuity equation for the liquid phase in the tube side can be expressed using equation (18) (Rezakazemi et al., 2019):

$$D_{CO2-tube}\left(\frac{1}{r}\frac{\partial}{\partial r}\left(\frac{r\,\partial C_{CO2-tube}}{\partial r}\right) + \frac{\partial^2 C_{CO2-tube}}{\partial z^2}\right) = V_{z-tube}\frac{\partial C_{CO2-tube}}{\partial z} + \frac{k_p a_p}{1-\emptyset} C_{CO2-tube} - C_{Sl} + R_i \tag{18}$$

The corresponding boundary conditions are as follows:

at $z = 0 C_{Solvent-tube} = C_{0-solvent}$ and $C_{CO2-tube} = 0$ (a)

at $z = H$ $\frac{\partial^2 C_{CO2-Tube}}{\partial z^2} = 0$ (b)

at $r = 0$ $\frac{\partial C_{CO2-Tube}}{\partial z} = 0$ (c)

at $r = r_1$ $C_{CO2-memb} = C_{CO2-tube}.m_{CO2}$ (d)

The boundary conditions for solving the governing equations of the shell, tube and membrane sides are summarized in **Table 3**.

3.3. CO_2 + MDEA + KLys + H_2O reaction mechanism

Zwitterion mechanism was used to interpret the CO_2-MDEA-KLys chemical reaction (Caplow, 1968). This mechanism includes the formation of a chemical intermediate expressed by equation (26) and carbamate formation which takes place by zwitterion deprotonation using fundamental bases such as amine groups, H_2O and OH^- (equation (24)) (Caplow, 1968). The reaction between CO_2 and MDEA + KLys solution can be exprexxed as given in equations (19-26).

$$^{+}H_3NR_2R_1CHNHCOO^- + H_2O \leftrightarrow {}^{+}H_3NR_2R_1CHNH_2 + HCO_3^- \tag{19}$$

$$LysH^+ \leftrightarrow LysH + H^+ \tag{20}$$

$$^{-}OOCHNR_2R_1CHNH_2 + H_2O \leftrightarrow H_2NR_2R_1CHNH_2 + HCO_3^- \tag{21}$$

$$LysH \leftrightarrow Lys^- + H^+ \tag{22}$$

$$MDEAH^+ \leftrightarrow MDEA + H^+ \tag{23}$$

$$H_2O + CO_2 \leftrightarrow H^+ + HCO_3^- \tag{24}$$

$$H_2O \leftrightarrow H^+ + OH^- \tag{25}$$

$$HCO_3^- \leftrightarrow H^+ + CO_3^{2-} \tag{26}$$

It should be noted that the overall rate of CO_2 absorption in a mixed solvent is the combined rate contribution of CO_2 with each solvent (Benamor et al., 2016; Mondal et al., 2017). In the case of CO_2 absorption in MDEA + KLys solution, the overall reaction can be attributed to the reaction between CO_2 and MDEA in parallel with the reaction of CO_2 with KLys, which is expressed using equation (27).

$$r_{CO2-solvent} = R_{CO_2} - KLys + R_{CO_2} - MDEA \tag{27}$$

The reaction of CO_2 with aqueous MDEA follows a pseudo-first-order reaction kinetics as given in equation (28) (Kierzkowska-Pawlak and Chacuk, 2010):

$$R_{CO_2-MDEA} = k_{MDEA}\ [CO_2]\ [MDEA] \tag{28}$$

For the reaction of CO_2 with KLys solution, a mechanism was proposed (Shen et al., 2016) using equation (29).

$$R_{CO_2-KLys} = k_{KLys}\ [CO_2]\ [KLys] \tag{29}$$

Whereby the reaction rate constants of k_{MDEA} and k_{KLys} given in equations (30) and (31) were taken from (Kierzkowska-Pawlak and Chacuk, 2010) and (Shen et al., 2016), respectively.

$$k_{MDEA} = 2.07 \times 10^9 \exp\left(\frac{-5912.7}{T}\right) \tag{30}$$

$$k_{Lys} = 2.778 \times 10^{13} \exp\left(-\frac{6138}{T}\right) \tag{31}$$

From equations (30) and (31), the overall reaction rate of CO_2 in MDEA + KLys solution can be written as (Eq. 32):

$$r_{CO2\_solvent} = -\left(2.778 \times 10^{13} \exp\left(-\frac{6138}{T_{gas}}\right) C_{KLys} + 2.07 \times 10^9 \exp\left(-\frac{5912.7}{T_{gas}}\right) C_{MDEA}\right) C_{CO2} \tag{32}$$

where T_{gas} is the gas temperature.

Table 3
Boundary conditions used in the simulation

Shell side	Membrane side	Tube side	Position
$\frac{\partial^2 C_{CO2-shell}}{\partial z^2} = 0$	*Insulated*	$C_{Solvent-tube} = C_{0-solvent}$	$Z = 0$
$C_{CO2-shell} = C_0$	*Insulated*	Convective flux	$Z = H$
	$C_{CO2-memb} = C_{CO2-tube}/m_{CO2}$	$C_{CO2-memb} = C_{CO2-tube} m_{CO2}$	$R = r_1$
$D_{CO2-shell}(\frac{\partial C_{CO2-shell}}{\partial r}) = D_{CO2-memb}(\frac{\partial C_{CO2-membrane}}{\partial r})$	$C_{CO2-memb} = C_{CO2-shell}$		$R = r_2$
$(\frac{\partial C_{CO2-shell}}{\partial r}) = 0$			$R = r_3$

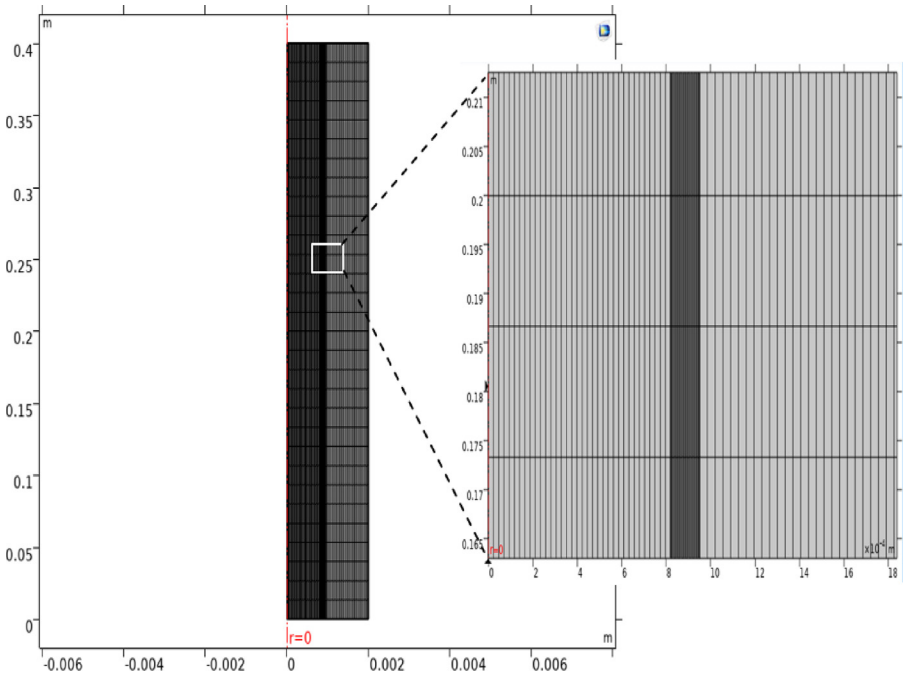

Fig. 4. Employed 3674 quad meshing discretization for developing computational simulation.

3.4. Mesh

Mapped meshing procedure is considered more appropriate compared to the other meshing techniques, because it can significantly reduce the computational discrepancies and improve the accuracy of software calculation. Moreover, this procedure is having excellent capability for covering the entire points of each domain (Eslami et al., 2011). In this work, all domains (shell, membrane, and tube) of HFMC have been aimed to be discretized into small dimension cells to study the effectiveness of parameter changes such as CO_2 concentration in each domain. Fig. 4 illustrates the triangular, corner refinement, boundary layers mesh in three main compartments of the HFMC.

It can be seen in the membrane domain that the implemented meshes are denser/smaller than the other segments due to the occurrence of gas/solvent contact and consequently CO_2-MDEA-KLys chemical reaction (Fig. 4).

3.5. Numerical solution

A set of coupled partial differential equations in the liquid, membrane and gas phases were achieved by the proposed mathematical model. To determine the liquid and gas concentration profile in the radial and axial directions, the set of differential equations should be solved simultaneously. To study flow and concentration fields in the HFMC, the conservation of mass and momentum equations along with mass transport equations for steady-state flow in the laminar flow regime, were numerically solved using Laminar Flow and Transport of Diluted Species physics of COMSOL Multiphysics (COMSOL 5.6, *Comsol Inc.*, USA) software.

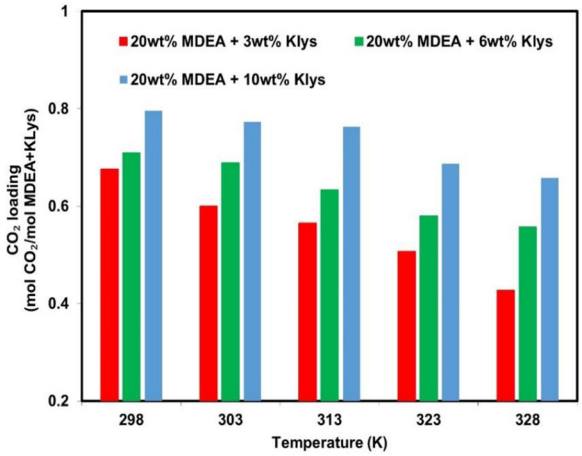

Fig. 5. The effect of temperature and KLys concentration on the CO_2 loading capacity of MDEA + KLys

4. Results and discussion

4.1. CO_2 loading capacity

The results of the CO_2 loading capacity of the MDEA + KLys solutions at different temperatures and KLys concentrations are shown in Fig. 5. The CO_2 loading capacity of MDEA + KLys solution was assessed by varying the temperature from 298.15 K to 328.15 K. It can be seen in Fig. 5 that the CO_2 loading capacity decreases as the temperature

Table 4
The specification of the HFMR used in model validation [54]

Parameter	Unit	Value
Inner tube diameter,(r_1)	mm	0.22
Outer tube diameter, (r_2)	mm	0.3
Module inner diameter, (R)	mm	63.5
Total number of fibers (**n**)	-	3600
Fiber porosity, (ϵ)	-	0.25
Fiber tortuosity (τ)	-	4
Inner shell diameter, (d)	mm	0.529
Module length, (L)	cm	25

increases. This can be attributed to the fact that most of the reactions involved in CO_2 absorption are reversible. As a result, when temperature is increased, equilibrium shifts in the backward direction and thus causing a decrease in CO_2 loading. Moreover, the desorption of CO_2 also takes place at high temperatures, however, this is natural because generally the solubility of various gases reduces with any rise in temperature (Balsora and Mondal, 2011).

Although the reactions between CO_2 and MDEA solution are stoichiometrically limited to 0.5 (mol CO_2/mol amine), the CO_2 loading capacity of MDEA + H_2O system can exceed this limit by the addition of an amine with high absorption capacity. Generally, the amino groups in the structure of absorbents are the main species reacting with CO_2 (Li et al., 2019). Therefore, more amino groups in the solutions can lead to greater absorption capacity. Lysine has two amino groups in its structure including α-amine group and ϵ-amine group that react with CO_2 and subsequently create a high CO_2 loading capacity of between 1 and 1.5 (mol CO_2/mol amine) (Shen et al., 2017).

The effect of the addition of KLys on CO_2 loading capacity of MDEA solution in terms of CO_2 loading capacity was investigated as well. The CO_2 loading capacity of MDEA + KLys system increases with increasing KLys concentration in the solution, where the highest CO_2 loading capacity, for different temperatures, was achieved for 20 wt.% MDEA + 10 wt.% KLys. Therefore, 20 wt.% MDEA + 10 wt.% KLys solution was selected for further investigation in this study and is being referred to herein after as MDEA + KLys solution.

4.2. Model validation

To the best of our knowledge, there is no experimental data on CO_2 removal efficiency of MDEA + KLys solution in the literature. Therefore, in order to validate the developed model, the simulation results for 0.5 $kmol/m^3$ of pristine MDEA at 298 K were compared to those reported in the literature (Rezakazemi et al., 2011). The specifications of the HFMR which were used for model validation presented in Table 4.

The verification process was performed through normalized CO_2 concentration using equation (33):

$$\eta = \left(\frac{C}{C_t}\right) \tag{33}$$

where C denotes the CO2 concentration in the gas phase ($molm^{(-3)}$) and C_t is the total concentration of inflow CO_2 ($molm^{(-3)}$).

It can be seen in **Fig. 6** that there is a good agreement between the simulation and experimental results with the Mean Squared Error (MSE) of 0.001 and the Average Relative Error (ARE) of about 4%, which actually verified the developed model.

4.3. Distribution of CO_2 concentration

The feed gas flows from the top of the contactor, at $z = H$, where the CO_2 concentration is postulated to be maximum at $z/L = H$. The solvent flows from the bottom of the contactor, at $z = 0$, where the CO_2 concentration is zero. The axial CO_2 concentration profile along the membrane module is illustrated in **Fig. 7a**.

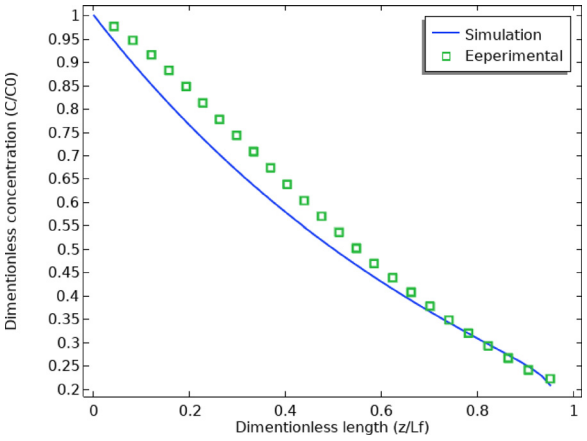

Fig. 6. Model validation with the experimental data adopted from (Rezakazemi et al., 2011); CO_2 inlet concentration = 50 vol.%, MDEA concentration =10 $wt\%$, T = 298 K.

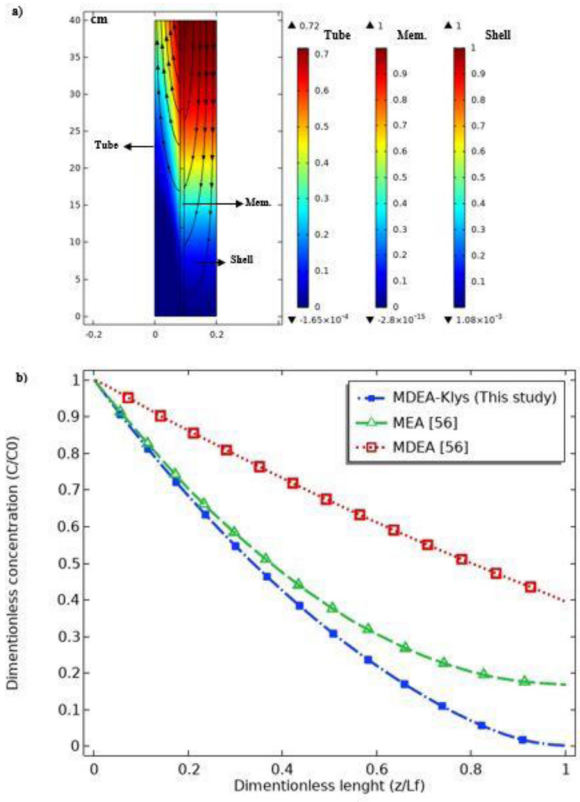

Fig. 7. (a) CO_2 normalized concentration distribution through the HFMC; (b) CO_2 normalized concentration profile along the HFMC (gas flow rate = 6 L/hr, solvent flow rate = 1.5 $L/hr, T_{gas}$ = 298 K, C_0 = 1400 ppm, C_s = 30 $wt\%$).

According to the streamlines, CO_2 from bulk gas is transferred toward the membrane pores due to partial pressure (concentration difference). At the entrance of the module, the concentration decline was sharper, due to higher driving force and contact area, and thereafter decreased gradually.

The dimensionless concentration (C/C_o) for MDEA + KLys, MEA and MDEA solutions are shown in **Fig. 7b**. In general, lower dimensionless concentration means higher CO_2 removal efficiency. It can be seen in **Fig. 7b** that the final dimensionless concentration for MDEA + KLys solution is lower compared to MEA and MDEA solutions, as most widely

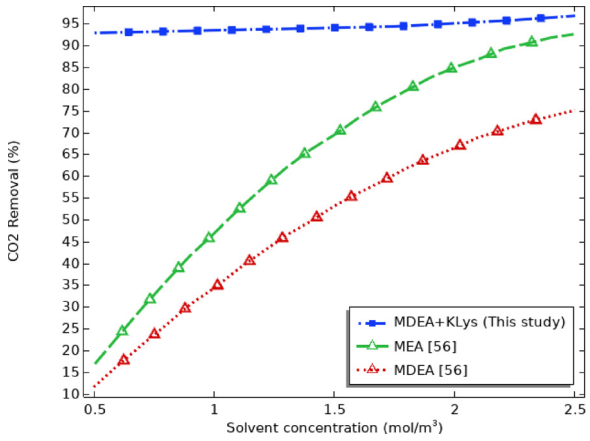

Fig. 8. Effect of solvent concentration on the CO_2 removal efficiency (gas flow rate = 6 L/hr, C_0 = 1400 ppm, solvent flow rate = 1.5 L/hr, $T_{gas} = 298\ K$)

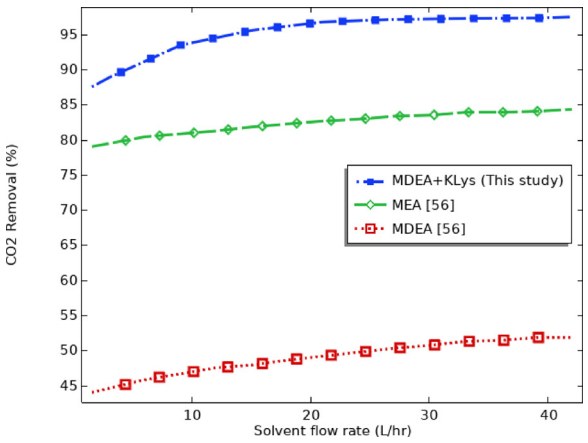

Fig. 9. Effect of solvent flow rate on the CO_2 removal efficiency (gas flow rate = 6 $L/hr, T_{gas} = 298\ K, C_0 = 1400\ ppm, C_s = 30wt\%$)

used solvents for CO_2 capture in industry, meaning better CO_2 absorption performance.

4.4. Effect of solvent concentration

The effect of solvent concentration on the CO_2 removal efficiency of MDEA + KLys, MDEA and MEA solutions is shown in **Fig. 8**.

It can be observed in Fig. 8 that with increasing solvent concentration, the CO_2 removal efficiency of all solutions significantly increases except for the MDEA + KLys that increases slightly. This could be considered as an additional advantage of MDEA + KLys solution compared to MDEA and MEA, where lower concentrations can be used which will result in lower viscosity, corrosion rate along with operational costs associated with CO_2 capture process. As expected, the CO_2 removal efficiency increases with increasing solvent concentration, which could be attributed to the availability of more molecules to react with CO_2. However, for MDEA + KLys solution with high KLys concentrations, a solid product is formed and leads to a decrease in CO_2 absorption capacity. This is one of the main challenges associated with amino acid salts where precipitation occurs, especially at high concentrations (Garg et al., 2017). MDEA + KLys solution showed better CO_2 removal efficiency (~96%) compared to MEA (~80%) and MDEA (~78%) under similar conditions.

4.5. Effect of solvent flow rate

The effect of solvent flow rate, in non-wetting mode, on the CO_2 removal efficiency is shown in **Fig. 9**. At low liquid flow rates, the CO_2 removal increases with increasing solvent flow rate, but it reaches a constant value at a certain flow rate (**Fig. 9**).

For example, for MDEA + KLys solution, increasing the liquid flow rate from 6 to 40 L/hr enhanced the CO_2 removal efficiency from ~86% to ~96%. However, increasing the liquid flow rate larger than 30 L/hr did not have a significant effect on the CO_2 removal efficiency. A similar trend was observed for other solvents. This can be attributed to chemical reaction between CO_2 and amine solvents, where the main mass transfer resistance is in the gas phase with respect to the liquid phase mass transfer resistance, which is not significant. It is worth mentioning that increasing the solvent flow rate enhances the concentration gradients of absorbed CO_2 in the liquid phase. This is due to high active reactant molecules of solvent, which improves the CO_2 removal efficiency.

4.6. Effects of gas flow rate

The effect of gas flow rate on the CO_2 removal efficiency is shown in **Fig. 10**. The CO_2 removal efficiency decreases as gas flow rate increases. However, this reduction for MDEA + KLys solvent is much lower than the ones in the MEA and MDEA. The CO_2 removal efficiency of MDEA + KLys was reduced from ~96% to ~68% while for the MEA and MDEA decreased to ~28% and ~17% respectively, as the gas flow rate increases.

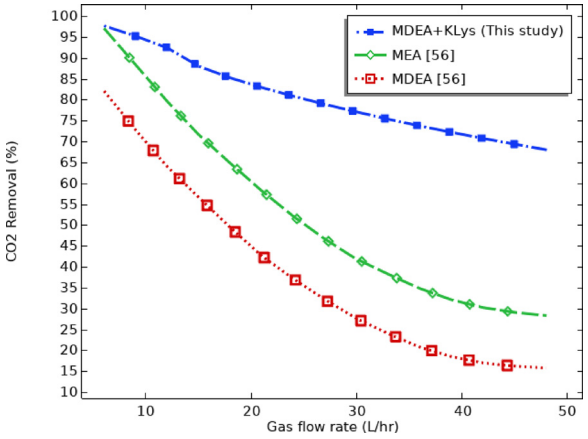

Fig. 10. Effect of gas flow rate on the CO_2 removal efficiency (solvent flow rate = 1.5 $L/hr, T_{gas} = 298\ K, C_0 = 1400\ ppm, C_s = 30wt\%$)

At lower gas flow rates, CO_2 removal efficiency is higher which could be related to higher CO_2 diffusivity into the solution. Furthermore, the gas-phase residence time decreases with increasing gas flow rate in the HFMC, thus leading to a reduction in CO_2 removal efficiency (Saidi, 2017).

4.7. Effect of ZIF-8

The effect of ZIF-8 loading amount on the CO_2 removal efficiency is shown in **Fig. 11**. It is observed that with increasing ZIF-8 concentration, CO_2 removal first increases and then decreases after the loading amount was more than 0.4 wt.%. However, such CO_2 removal increase is marginal and therefore any further increase in loading is not beneficial.

The highest CO_2 removal efficiency was achieved for 0.4 wt.% of ZIF-8. Although, increasing the loading amount theoretically increases CO_2 removal, but it can lead to particle agglomeration which can block the pores of the membrane, resulting in a decrease in the gas-liquid interface area and lower removal rate. In addition, the ZIF-8 loading affects the stability of the nano-absorbent, which can reduce the absorption efficiency of the nano-absorbent (Yu et al., 2019).

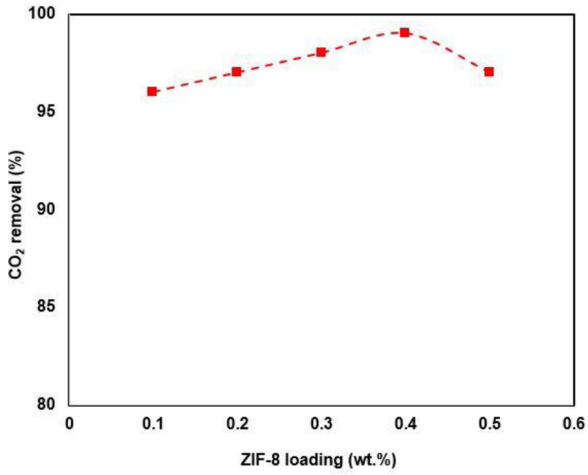

Fig. 11. The effect of ZIF-8 loading amount on the CO_2 removal efficiency of the MDEA + KLys + ZIF-8

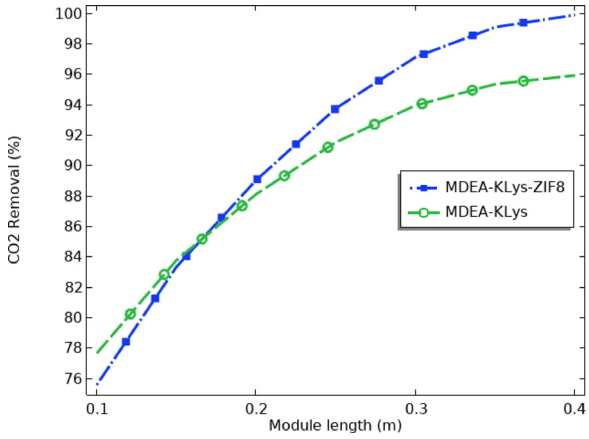

Fig. 12. CO_2 removal efficiency of versus module length for MDEA + KLys and MDEA + KLys + ZIF-8 solutions (gas flow = 6 L/hr, solvent flow rate =1.5 L/hr, T_{gas} = 298 $K, \emptyset = 0.4$ $wt.\%, C_s = 30$ $wt\%$)

The CO_2 removal efficiency of MDEA + KLys absorbent and MDEA + KLys + ZIF-8 nano-absorbent along the module is shown in Fig. 12. In general, the CO_2 removal efficiency increases with increasing the fiber length, which could be due to an increase in the contact time and area of the gas and liquid phase.

The CO_2 removal efficiency of MDEA + KLys is larger than that of MDEA + KLys + ZIF-8 at the beginning of the module (< 0.2 m), while it gets higher for the rest of the reactor, where it reached to ~99% for MDEA + KLys + ZIF-8. This increase in CO_2 removal efficiency could be attributed to several reasons, including enhancement of mass transfer coefficient, additional reactions of CO_2 in the presence of ZIF-8 and zwitterion mechanism. There are several mechanisms that can be considered for the improvement in the mass transfer coefficient, which include hydrodynamic and bubble breaking effects in the presence of nanomaterials (Yu et al., 2019).

In order to further investigate the separation performance of the MDEA + KLys + ZIF-8 nano-absorbent, its CO_2 removal efficiency for different gas flow rates were compared with other nano-absorbents and shown in Fig. 13. It is seen that increasing the gas flow rate resulted in the reduction of the residence time of CO_2 in the membrane contactor. Furthermore, increasing the gas flow rate also resulted in the reduction of the amount of CO_2 molecules that could permeate through the membrane. The MDEA + KLys + ZIF-8 nano-absorbent exhibited higher CO_2 removal efficiency compared to other nano-absorbents.

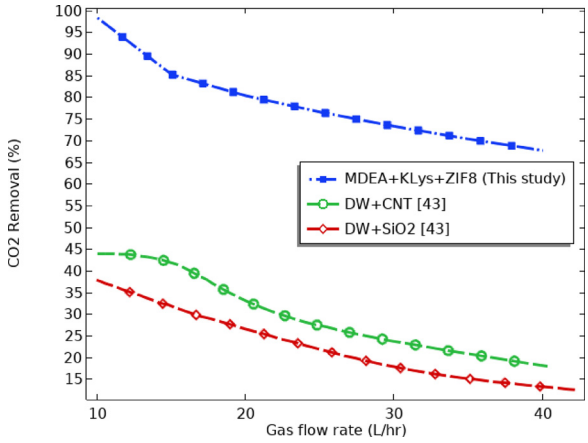

Fig. 13. Effect of gas flow rate on the efficiency of CO_2 removal for MDEA + KLys + ZIF-8

(solvent flow rate = 1.5 L/hr, T_{gas} = 298 K, C_0 = 1400 ppm,C_s = 30 $wt\%$)

Additionally, Fig. 13 reveals that the CO_2 removal efficiency of DW-CNT and DW-SiO_2 nano-absorbents was almost constant at high gas flow rates, which is due to negligible mass transfer resistance in the gas phase. The CO_2 removal of MDEA + KLys + ZIF-8 continues to be higher than the other nano-absorbents at high gas flow rates.

5. Conclusion

In this study, MDEA + KLys and MDEA + KLys + ZIF-8 solutions are proposed as novel absorbents for CO_2 absorption. The CO_2 loading capacity of MDEA + KLys solutions was measured using a gas absorption setup at different concentrations and temperatures. It was found that CO_2 loading capacity of the solutions increases with increasing KLys concentration in the solution. The CO_2 removal performance of the MDEA + KLys solution was investigated through CFD simulations in a HFMC. The results indicated that MDEA + KLys solution has a better CO_2 removal performance compared to pristine MDEA and MEA. Furthermore, the CO_2 removal efficiency increases as solvent concentration, solvent flow rate and module length increase. However, it decreases with increasing gas flow rate. Given these results, the ZIF-8 was then incorporated into the MDEA + KLys solution and CO_2 removal performance of the MDEA + KLys + ZIF-8 nano-absorbent was evaluated. The MDEA + KLys + ZIF-8 exhibited higher CO_2 removal efficiency compared to pristine MDEA + KLys solution. The results further showed that the CO_2 absorption performance of ZIF-8 nano-absorbent was higher than that of other nano absorbents, such as the CNT. Therefore, MDEA + KLys + ZIF-8 can be proposed as an appropriate alternative absorbent to remove CO_2 in gas-liquid hollow fiber membrane contactors.

Declaration of Competing Interest

The authors declare that they have no known competing financial interests or personal relationships that could have appeared to influence the work reported in this paper.

CRediT authorship contribution statement

Saber Kiani: Conceptualization, Methodology, Validation, Formal analysis, Investigation, Writing – original draft. **Ahmad Taghizade:** Conceptualization, Methodology, Validation, Formal analysis, Investigation, Writing – original draft. **Rouzbeh Ramezani:** Conceptualization, Investigation, Writing – review & editing. **Renzo Di Felice:** Conceptualization, Resources, Investigation, Writing – review & editing.

Gomotsegang Fred Molelekwa: Investigation, Writing – review & editing. **Saeed Mazinani:** Conceptualization, Resources, Supervision, Writing – review & editing.

References

Alper, E., Wichtendahl, B., Deckwer, W.-D., 1980. Gas absorption mechanism in catalytic slurry reactors. Chemical Engineering Science 35 (1-2), 217–222. doi:10.1016/0009-2509(80)80090-X.

Bahmanyar, A., Khoobi, N., Moharrer, M.M.A., Bahmanyar, H., 2014. Mass transfer from nanofluid drops in a pulsed liquid–liquid extraction column. Chemical Engineering Research and Design 92 (11), 2313–2323. doi:10.1016/j.cherd.2014.01.024.

Balsora, H.K., Mondal, M.K., 2011. Solubility of CO2 in an aqueous blend of diethanolamine and trisodium phosphate. Journal of Chemical & Engineering Data 56 (12), 4691–4695. doi:10.1021/je2006677.

Benamor, A., Al-Marri, M.J., Khraisheh, M., Nasser, M.S., Tontiwachwuthikul, P., 2016. Reaction kinetics of carbon dioxide in aqueous blends of N-methyldiethanolamine and glycine using the stopped flow technique. Journal of Natural Gas Science and Engineering 33, 186–195. doi:10.1016/j.jngse.2016.04.063.

Caplow, M., 1968. Kinetics of carbamate formation and breakdown. Journal of the American Chemical Society 90 (24), 6795–6803. doi:10.1021/ja01026a041.

Eslami, S., Mousavi, S.M., Danesh, S., Banazadeh, H., 2011. Modeling and simulation of CO2 removal from power plant flue gas by PG solution in a hollow fiber membrane contactor. Advances in Engineering Software 42 (8), 612–620. doi:10.1016/j.advengsoft.2011.05.002.

Fang, M., Yi, N., Di, W., Wang, T., Wang, Q., 2020. Emission and control of flue gas pollutants in CO2 chemical absorption system–a review. International Journal of Greenhouse Gas Control 93, 102904. doi:10.1016/j.ijggc.2019.102904.

Feron, P.H., Jansen, A.E., 2002. CO2 separation with polyolefin membrane contactors and dedicated absorption liquids: performances and prospects. Separation and Purification Technology 27 (3), 231–242. doi:10.1016/S1383-5866(01)00207-6.

Garg, S., Murshid, G., Mjalli, F.S., Ali, A., Ahmad, W., 2017. Experimental and correlation study of selected physical properties of aqueous blends of potassium sarcosinate and 2-piperidineethanol as a solvent for CO2 capture. Chemical Engineering Research and Design 118, 121–130. doi:10.1016/j.cherd.2016.12.013.

Ghasem, N., 2019a. Chemical absorption of CO2 enhanced by nanoparticles using a membrane contactor: Modeling and simulation. Membranes 9 (11), 150. doi:10.3390/membranes9110150.

Ghasem, N., 2019b. Modeling and Simulation of CO2 Absorption Enhancement in Hollow-Fiber Membrane Contactors using CNT–Water-Based Nanofluids. Journal of Membrane Science and Research 5 (4), 295–302. doi:10.22079/jmsr.2019.100177.1239.

Golkhar, A., Keshavarz, P., Mowla, D., 2013. Investigation of CO2 removal by silica and CNT nanofluids in microporous hollow fiber membrane contactors. Journal of membrane science 433, 17–24. doi:10.1016/j.memsci.2013.01.022.

Happel, J., 1959. Viscous flow relative to arrays of cylinders. AIChE Journal 5 (2), 174–177. doi:10.1002/aic.690050211.

Hara, N., 2016. ZIF-8 Membrane. In: Drioli, E., Giorno, L. (Eds.), Encyclopedia of Membranes. Springer Berlin Heidelberg, Berlin, Heidelberg, pp. 2064–2067. doi:10.1007/978-3-662-44324-8_1988.

Hashemi, F., Rowshanzamir, S., Rezakazemi, M., 2012. CFD simulation of PEM fuel cell performance: effect of straight and serpentine flow fields. Mathematical and Computer Modelling 55 (3-4), 1540–1557. doi:10.1016/j.mcm.2011.10.047.

He, F., Wang, T., Fang, M., Wang, Z., Yu, H., Ma, Q., 2017. Screening test of amino acid salts for CO2 absorption at flue gas temperature in a membrane contactor. Energy & Fuels 31 (1), 770–777. doi:10.1021/acs.energyfuels.6b02578.

Hong, B., Liu, L., Wang, S.-M., Han, Z.-B., 2016. Facile synthesis of ZIF-8/ZnO/polyoxometalate ternary composite materials for efficient and rapid removal of cationic organic dye. Journal of Cluster Science 27 (2), 563–571. doi:10.1007/s10876-015-0955-x.

Huang, S.-M., Zhang, L.-Z., 2013. Researches and trends in membrane-based liquid desiccant air dehumidification. Renewable and Sustainable Energy Reviews 28, 425–440. doi:10.1016/j.rser.2013.08.005.

Hunter-Sellars, E., Saenz-Cavazos, P.A., Houghton, A.R., McIntyre, S.R., Parkin, I.P., Williams, D.R., 2021. Sol–Gel Synthesis of High-Density Zeolitic Imidazolate Framework Monoliths via Ligand Assisted Methods: Exceptional Porosity, Hydrophobicity, and Applications in Vapor Adsorption. Advanced Functional Materials 31 (5), 2008357. doi:10.1002/adfm.202008357.

Irani, V., Maleki, A., Tavasoli, A., 2019. CO2 absorption enhancement in graphene-oxide/MDEA nanofluid. Journal of environmental chemical engineering 7 (1), 102782. doi:10.1016/j.jece.2018.11.027.

Kang, D., Park, S., Jo, H., Min, J., Park, J., 2013. Solubility of CO2 in amino-acid-based solutions of (potassium sarcosinate),(potassium alaninate+ piperazine), and (potassium serinate+ piperazine). Journal of Chemical & Engineering Data 58 (6), 1787–1791. doi:10.1021/je4001813.

Kierzkowska-Pawlak, H., Chacuk, A., 2010. Kinetics of carbon dioxide absorption into aqueous MDEA solutions. Ecol. Chem. Eng. S 17 (4), 463–475.

Kumar, P.S., Hogendoorn, J., Feron, P., Versteeg, G., 2001. Density, viscosity, solubility, and diffusivity of N2O in aqueous amino acid salt solutions. Journal of Chemical & Engineering Data 46 (6), 1357–1361. doi:10.1021/je010043a.

Li, Y., Tan, Z., Zhang, Z., Hu, X., 2019. Experimental studies on carbon dioxide absorption using potassium carbonate solutions with amino acid salts. Separation and Purification Technology 219, 47–54. doi:10.1016/j.seppur.2019.03.010.

Li, Y., Zhou, K., He, M., Yao, J., 2016. Synthesis of ZIF-8 and ZIF-67 using mixed-base and their dye adsorption. Microporous and Mesoporous Materials 234, 287–292. doi:10.1016/j.micromeso.2016.07.039.

Mazinani, S., Ramazani, R., Samsami, A., Jahanmiri, A., Van der Bruggen, B., Darvishmanesh, S., 2015. Equilibrium solubility, density, viscosity and corrosion rate of carbon dioxide in potassium lysinate solution. Fluid Phase Equilibria 396, 28–34. doi:10.1016/j.fluid.2015.03.031.

Mazinani, S., Samsami, A., Jahanmiri, A., Sardarian, A., 2011. Solubility (at low partial pressures), density, viscosity, and corrosion rate of carbon dioxide in blend solutions of monoethanolamine (MEA) and sodium glycinate (SG). Journal of Chemical & Engineering Data 56 (7), 3163–3168. doi:10.1021/je2002418.

Mohebbi-Kalhori, D., Sadeghi, J., Shahraki, F., Shahraki, H., 2020. Enhancement of CO2 mass transfer using SiO2 nanoparticles in an aqueous a-MDEA solution for CO2 absorption process. Transp Phenom Nano Micro Scales 8 (2), 117–125. doi:10.22111/TPNMS.2020.32717.1183.

Mondal, B.K., Bandyopadhyay, S.S., Samanta, A.N., 2017. Kinetics of CO2 absorption in aqueous hexamethylenediamine blended N-methyldiethanolamine. Industrial & Engineering Chemistry Research 56 (50), 14902–14913. doi:10.1021/acs.iecr.7b02744.

Nagy, E., Feczkó, T., Koroknai, B., 2007. Enhancement of oxygen mass transfer rate in the presence of nanosized particles. Chemical Engineering Science 62 (24), 7391–7398. doi:10.1016/j.ces.2007.08.064.

Nakhjiri, A.T., Heydarinasab, A., 2020. Efficiency evaluation of novel liquid potassium lysinate chemical solution for CO2 molecular removal inside the hollow fiber membrane contactor: Comprehensive modeling and CFD simulation. Journal of Molecular Liquids 297, 111561. doi:10.1016/j.molliq.2019.111561.

Peng, D.-Y., Robinson, D.B., 1976. A new two-constant equation of state. Industrial & Engineering Chemistry Fundamentals 15 (1), 59–64. doi:10.1021/i160057a011.

Peyravi, A., Keshavarz, P., Mowla, D., 2015. Experimental investigation on the absorption enhancement of CO2 by various nanofluids in hollow fiber membrane contactors. Energy & Fuels 29 (12), 8135–8142. doi:10.1021/acs.energyfuels.5b01956.

Portugal, A., Sousa, J., Magalhães, F., Mendes, A., 2009. Solubility of carbon dioxide in aqueous solutions of amino acid salts. Chemical Engineering Science 64 (9), 1993–2002. doi:10.1016/j.ces.2009.01.036.

Prasher, R., Bhattacharya, P., Phelan, P.E., 2005. Thermal conductivity of nanoscale colloidal solutions (nanofluids). Physical review letters 94 (2), 025901. doi:10.1103/PhysRevLett.94.025901.

Ramezani, R., Di, Felice, R., 2019. Kinetics study of CO2 absorption in potassium carbonate solution promoted by diethylenetriamine. Green Energy & Environment doi:10.1016/j.gee.2019.11.004.

Ramezani, R., Mazinani, S., Di, Felice, R., 2018. Characterization and kinetics of CO2 absorption in potassium carbonate solution promoted by 2-methylpiperazine. Journal of Environmental Chemical Engineering 6 (2), 3262–3272. doi:10.1016/j.jece.2018.05.019.

Ramezani, R., Mazinani, S., Di, Felice, R., 2020. State-of-the-art of CO2 capture with amino acid salt solutions. Reviews in Chemical Engineering 1. doi:10.1515/revce-2020-0012, (ahead-of-print).

Rezakazemi, M., 2018. CFD simulation of seawater purification using direct contact membrane desalination (DCMD) system. Desalination 443, 323–332. doi:10.1016/j.desal.2017.12.048.

Rezakazemi, M., Darabi, M., Soroush, E., Mesbah, M., 2019. CO2 absorption enhancement by water-based nanofluids of CNT and SiO2 using hollow-fiber membrane contactor. Separation and Purification Technology 210, 920–926. doi:10.1016/j.seppur.2018.09.005.

Rezakazemi, M., Niazi, Z., Mirfendereski, M., Shirazian, S., Mohammadi, T., Pak, A., 2011. CFD simulation of natural gas sweetening in a gas–liquid hollow-fiber membrane contactor. Chemical Engineering Journal 168 (3), 1217–1226. doi:10.1016/j.cej.2011.02.019.

Rezakazemi, M., Shirazian, S., Ashrafizadeh, S.N., 2012. Simulation of ammonia removal from industrial wastewater streams by means of a hollow-fiber membrane contactor. Desalination 285, 383–392. doi:10.1016/j.desal.2011.10.030.

Saidi, M., 2017. Mathematical modeling of CO2 absorption into novel reactive DEAB solution in hollow fiber membrane contactors; kinetic and mass transfer investigation. Journal of membrane science 524, 186–196. doi:10.1016/j.memsci.2016.11.028.

Shen, S., Yang, Y.-n., Bian, Y., Zhao, Y., 2016. Kinetics of CO2 absorption into aqueous basic amino acid salt: potassium salt of lysine solution. Environmental science & technology 50 (4), 2054–2063. doi:10.1021/acs.est.5b04515.

Shen, S., Zhao, Y., Bian, Y., Wang, Y., Guo, H., Li, H., 2017. CO2 absorption using aqueous potassium lysinate solutions: vapor–liquid equilibrium data and modelling. The Journal of Chemical Thermodynamics 115, 209–220. doi:10.1016/j.jct.2017.07.041.

Shirazian, S., Marjani, A., Rezakazemi, M., 2012a. Separation of CO 2 by single and mixed aqueous amine solvents in membrane contactors: fluid flow and mass transfer modeling. Engineering with Computers 28 (2), 189–198. doi:10.1007/s00366-011-0237-7.

Shirazian, S., Rezakazemi, M., Marjani, A., Rafivahid, M.S., 2012b. Development of a mass transfer model for simulation of sulfur dioxide removal in ceramic membrane contactors. Asia-Pacific Journal of Chemical Engineering 7 (6), 828–834. doi:10.1002/apj.641.

Song, H.-J., Park, S., Kim, H., Gaur, A., Park, J.-W., Lee, S.-J., 2012. Carbon dioxide absorption characteristics of aqueous amino acid salt solutions. International Journal of Greenhouse Gas Control 11, 64–72. doi:10.1016/j.ijggc.2012.07.019.

Sumin, L., Min, X., Yan, S., Xiangjun, D., 2013. Experimental and theoretical studies of CO2 absorption enhancement by nano-Al2O3 and carbon nanotube particles. Chinese Journal of Chemical Engineering 21 (9), 983–990. doi:10.1016/S1004-9541(13)60550-9.

Wang, J., Liu, Q., 2014. An efficient one-step condensation and activation strategy to synthesize porous carbons with optimal micropore sizes for highly selective CO 2 adsorption. Nanoscale 6 (8), 4148–4156. doi:10.1039/C3NR05825E.

Yang, Y., Ge, L., Rudolph, V., Zhu, Z., 2014. In situ synthesis of zeolitic imidazolate frameworks/carbon nanotube composites with enhanced CO 2 adsorption. Dalton Transactions 43 (19), 7028–7036. doi:10.1039/C3DT53191K.

Yu, W., Wang, T., Park, A.-H.A., Fang, M., 2019. Review of liquid nano-absorbents for enhanced CO 2 capture. Nanoscale 11 (37), 17137–17156. doi:10.1039/C9NR05089B.

Zhang, Y., Wang, H., Liang, S., Xu, M., Liu, W., Li, S., Zhang, R., Nielsen, C.P., Bi, J., 2014. Temporal and spatial variations in consumption-based carbon dioxide emissions in China. Renewable and Sustainable Energy Reviews 40, 60–68. doi:10.1016/j.rser.2014.07.178.

Zhang, Z., Cai, J., Chen, F., Li, H., Zhang, W., Qi, W., 2018a. Progress in enhancement of CO2 absorption by nanofluids: A mini review of mechanisms and current status. Renewable energy 118, 527–535. doi:10.1016/j.renene.2017.11.031.

Zhang, Z., Li, Y., Zhang, W., Wang, J., Soltanian, M.R., Olabi, A.G., 2018b. Effectiveness of amino acid salt solutions in capturing CO2: A review. Renewable and Sustainable Energy Reviews 98, 179–188. doi:10.1016/j.rser.2018.09.019.

Zhao, Y., Bian, Y., Li, H., Guo, H., Shen, S., Han, J., Guo, D., 2017. A comparative study of aqueous potassium lysinate and aqueous monoethanolamine for postcombustion CO2 capture. Energy & Fuels 31 (12), 14033–14044. doi:10.1021/acs.energyfuels.7b02800.